Supplementary On-Line Materials: Revised Manuscript 1101304

Supplementary On-Line Figure Captions:

Fig. S1. Two 3-D perspectives of event relocations at depth: the first from the NE and above a plane which is a best-fit plane to the 3-D pattern of best located events representing about two-thirds of the total number of events. The second view is from the SSE looking along strike.

Fig. S2. a) Shallow seismicity (< 20 km depth) 10 October 2002 through 30 June 2004 within 30 km of the North Lake Tahoe swarm. Pre-swarm activity has been processed at a higher magnitude detection threshold that post-swarm activity. Earthquakes shown are consistent with pre-swarm detection threshold level. Earthquakes are color coded; Red: pre-swarm; Green: 11 August 2003 to 2 June 2004 (prior to Mw 4.2); Yellow: post 2 June 2004 (includes Mw 4.2 earthquake and its aftershocks). b) All UNR catalog earthquakes within 30 km epicentral distance of swarm; Red: pre-swarm; Yellow; 11 August 2003 through 30 June 2004. c) Cumulative number of shallow (< 20 km depth) events from 1 October 2002 through 30 June 2004 shown at pre-swarm magnitude detection threshold level.

Fig. S3. Fault-plane solutions for deep crustal earthquakes. ($M_L > 1.5$). Two conjugate planes are determined from the seismic data, either being the true slip plane. The planes

are projected to the equatorial plane of an imaginary sphere around the hypocenter. First motions from the seismic stations are also projected onto this plane (+ for compression, º for dilatation).

Fig. S4. Composite P- and T- axes for the 24 focal mechanism solutions (earthquakes > M_L 1.5). The poles are plotted on a stereo-net projection of an imaginary sphere around each hypocenter.

Supplementary Text for Online View:

Earthquake Relocations:

Hypocenter locations were derived from program HYPODD (1-S) and a modified 1-D Sierra block velocity model (2-S). Prior to HYPODD locations, events were initially located with program FASTPONG (3-S) applying a set of stations corrections. HYPODD is a double-difference technique where event locations are derived based on their association with neighboring events and common station phase arrivals. Only catalog arrival times were used in the HYPODD location. The model was modified to eliminate the layer at 30 km depth that intersected the swarm (Table S1).

Table S1. Velocity Model

Vp	Depth(km)
5.5	0.0
6.2	10.0
6.8	20.0
7.5	40.0
8.0	47.0

Vp: P-wave velocity in km/sec. S-wave velocity is assumed to be $\frac{Vp}{\sqrt{3}}$.

Depth: Depth to top of layer with corresponding body wave velocity.

S-wave travel times are critical for depth control for the deep source area. Ten seismograph stations within one focal depth provide control on hypocenters depths. The final locations shown in Fig. 1 represent a subset of the best 1179 event locations from all 1601 events from 2003. "Best locations" were based on HYODD event travel-time residuals of less than 0.08 seconds and a minimum number of linked station pairs per event. Relative location errors are estimated to be ± 250 meters based on event root-mean-square travel time residuals, whereas errors in absolute depth estimates are more difficult to assess. The best located events have P-wave travel time residuals with respect to the velocity model for the closest stations of about 0.05 seconds. This translates to an absolute depth error of ± ~1.5 km for the best located events with respect to the modified Sierra model.

Modeling Focal Mechanisms:

In general, small magnitude events do not provide sufficient P-wave first motions for determining earthquake focal mechanisms. Since new digital instrumentation provides true ground motion in three dimensions, in principal, double-couple dislocation solutions can be determined from an event location with a single 3-component station. However, due to seismic noise at low ground motions at even the most sensitive instruments, the best approach is to supplement available first-motion information with reliable amplitude data in order to lower the magnitude threshold for determining double-couple focal

mechanism solutions. Focal mechanisms for the deep Tahoe events were determined using a grid search routine and a weighted combination of amplitude and first-motion data. Weights are controlled by the user so that either first-motion or body-wave amplitudes can be favored depending on quality of the amplitude information and the relative number and quality of P-wave first-motions. This is an interactive procedure similar to trained record analysts timing phase arrivals and developing regional earthquake catalogs.

Energy and Earthquake Size: The seismic moment is defined as $M_0 = \mu AD$, where μ is the shear modulus of the rock, *A* is the fault area, and *D* is the average slip on the fault. It is understood as the size of one couple of the moment of force (or internal torque) acting at the source. Seismic moment is correlated to seismic energy release E by the relation $E = \sigma M_0/\mu$ where σ is the average stress acting over the fault during rupture and μ is the rigidity. At low magnitudes log-moment is proportional to the local earthquake magnitude M_L by $\log_{10}(M_0) = M_L + c$. A (usually) good statistical relationship between the number of earthquakes and magnitude is $N(M_L) = 10^{a-b(M_L-M_r)}$, where M_r is an arbitrary reference magnitude. The summed moment release for earthquakes in a magnitude range ($M_1 \le M_L \le M_2$) is then $\Sigma M_0(M_1, M_2) = \int_{M_1}^{M_2} 10^{a-b(M_L-M_r)} 10^{c+M}\, dM_L$.

With these assumptions and correlations, it is clear that $\Sigma M_0(M_r - \Delta, M_r)$ is equal to $\Sigma M_0(M_r, M_r + \Delta)$ when b=1, and when b>1, $\Sigma M_0(M_r - \Delta, M_r)$ is larger. Because energy is proportional to moment, the same b-value threshold separates domains where energy release is dominated by small or by large earthquakes.

Additional GPS Analysis Details: Dual frequency carrier phase and pseudorange data were processed using the latest available release (November 2003) of the GIPSY OASIS II software (4-S) from the Jet Propulsion Laboratory (JPL). The data were automatically edited and then decimated to 5 minute intervals, and ionosphere-free linear combinations were formed. Precise point positions were estimated for stations individually by fixing satellite orbit and clock parameters (fiducial-free versions) to values derived from the International GPS Service Analysis Center at JPL. Estimated parameters included the station coordinates, station clock at each epoch (as white noise), zenith tropospheric delay as random walk noise, and tropospheric gradients. A 15-degree elevation mask was used. Carrier phase ambiguity resolution was then performed using a bootstrapping algorithm for the entire network, where the widelaning method using either pseudorange or ionospheric constraints was selected automatically based on formal errors (5-S). The resulting fiducial-free station coordinates from each day were transformed into ITRF2000 using parameter files from JPL. Station velocities and annual periodic signals were estimated using only data from 2000.0–2003.5 for two reasons: firstly to establish secular and seasonal motion prior to the transient event, as a basis for comparison with data after 2003.5, and secondly because the 3.5 yr span minimizes correlation between estimated velocities and seasonal signals (6-S). The regional filtering algorithm assumes that the 5 neighboring BARGEN stations were unaffected by the event causing the SLID displacement, which was justified *a posteriori* by the sub-millimeter estimated displacements at these stations. The scale of the formal errors was initialized by assuming a 10 mm white noise for the ionosphere-free carrier phase data and 1000 mm

for the pseudorange data at 5 minute intervals. These were then further scaled by a factor of 1.2 so that the resulting error bars were consistent with the residual coordinate scatter prior to 2003.5. The station coordinate time series were filtered by first rejecting daily solutions with scaled formal errors > 4 mm longitude and latitude or > 12 mm in height, and then rejecting weekly averages with <2 contributing days, or with a root mean square scatter of daily solutions during each week > 2 mm in the horizontal, or > 6 mm in height. The difference in mean coordinates between periods 2004.0–2004.5 and 2003.0–2003.5 were taken as displacement estimates in order to further reduce any residual effects of seasonal signals.

Static Surface Displacement Due to a Buried Tensile Fault: Here we focus on the tensile fault as a likely mechanism to explain both observed surface displacements and increased earthquake activity seen at north Lake Tahoe. The expressions for surface static displacements due to arbitrary buried faults are given in Okada (7-S). For a tensile fault buried at the point (0,0,*d*) in a homogeneous medium, the surface displacements are

$$u_x = (P/2\pi)\,(3xd^2/R^5)$$

$$u_y = (P/2\pi)\,(3yd^2/R^5)$$

$$u_z = (P/2\pi)\,(3dd^2/R^5)$$

where

P = potency = $U\cdot\,\Delta\Sigma$ in Okada's notation where U is displacement of the crack faces perpendicular to the crack surface and $\Delta\Sigma$ is the surface area of the crack

$$R = (x^2 + y^2 + d^2)^{1/2}$$

Note that potency is a volumetric measure, appropriate to a tensile crack with sill-like filling. From the three expressions for the three components of displacement, one sees that the geometry of the tensile fault (0,0,d) relative to the geodetic observation station at (x,y,0) is completely set by the u_i observations. Moreover, using the equivalency of the displacements and the geometry to within a constant, the potency can be solved for as

$$P = (2/3)\pi d^2_{[ux}{}^2 + u_y{}^2 + u_z{}^2]^{5/2}$$

Taking the observed u_i displacements as (3.1,4.9,7.9) mm from Fig. 3 and setting d = 30, we get $P = 3.7 \cdot 10^7$ m^3. For a density, $\rho = 2.8 \frac{g}{cm^3}$, and lower crustal S-wave velocity of, β = 3.9 km/sec, the lower crustal rigidity is, $\mu = 4.3 \cdot 10^{10}$ Pa. The equivalent seismic moment ($M_0 = \mu P$) is $1.5 \cdot 10^{18}$ N-m; Mw = 6.1.

Supplemental References:

(1-S.) F. Waldhauser, U. S. Geol. Survey Open-File Report 01-113 (2001).

(2-S.) M Savage, L Li., J. Eaton, C. Jones, J. Brune, Tectonics 13, 803 (1994).

(3-S.) Herrmann, R.B., Earthquake Notes, 50, 25 (1979).

(4-S.) J. Zumberge, M Heflin, D. Jefferson, M. Watkins, F. Webb, *J. Geophys. Res., 102*, 5005 (1997).

(5-S.) G. Blewitt, *J. Geophys. Res.Vol. 94*, No. B8, p. 10,187-10,283 (1989).

(6-S.) G. Blewitt, G., D. Lavallee, Journ. *Geophys. Res., 107*(B7), 10.1029/2001JB000570, (2002).

7-S.) Y. Okada, Bull. Seism. Soc. Am., 75, 1135 (1985).

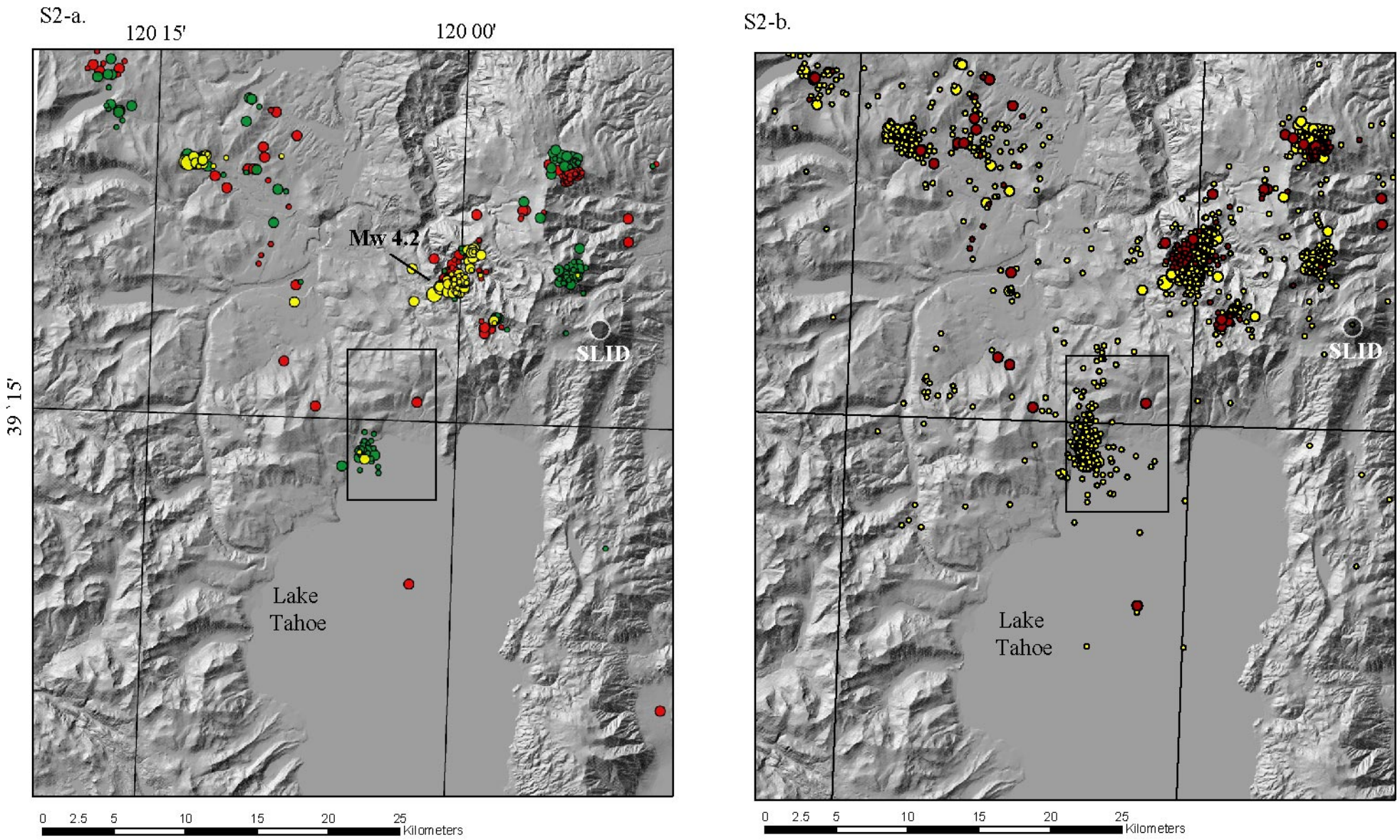
S2-a.
120 15'
120 00'
39 ` 15'
Mw 4.2
SLID
Lake
Tahoe
0 2.5 5 10 15 20 25
Kilometers
Legend
10/1/02 - 8/11/03
mag
0.8 - 1.0
1.1 - 3.0
3.1 - 5.0
8/12/03 - 6/2/04
mag
0.8 - 1.0
1.1 - 3.0
3.1 - 5.0
6/3/04 - 6/30/04
mag
0.8 - 1.0
1.1 - 3.0
3.1 - 5.0
grid_Project
Consistent Detection
Threshold
10/1/2002 - 6/30/2004
S2-b.
SLID
Lake
Tahoe
0 2.5 5 10 15 20 25
Kilometers
Legend
Pre-swarm
-0.1 - 1.0
1.1 - 3.0
3.1 - 5.0
Post-8/12/2003
-0.1 - 1.0
1.1 - 3.0
3.1 - 5.0
All Catalog Events
10/1/2002 - 6/30/2004

Figure S2

S2-c.

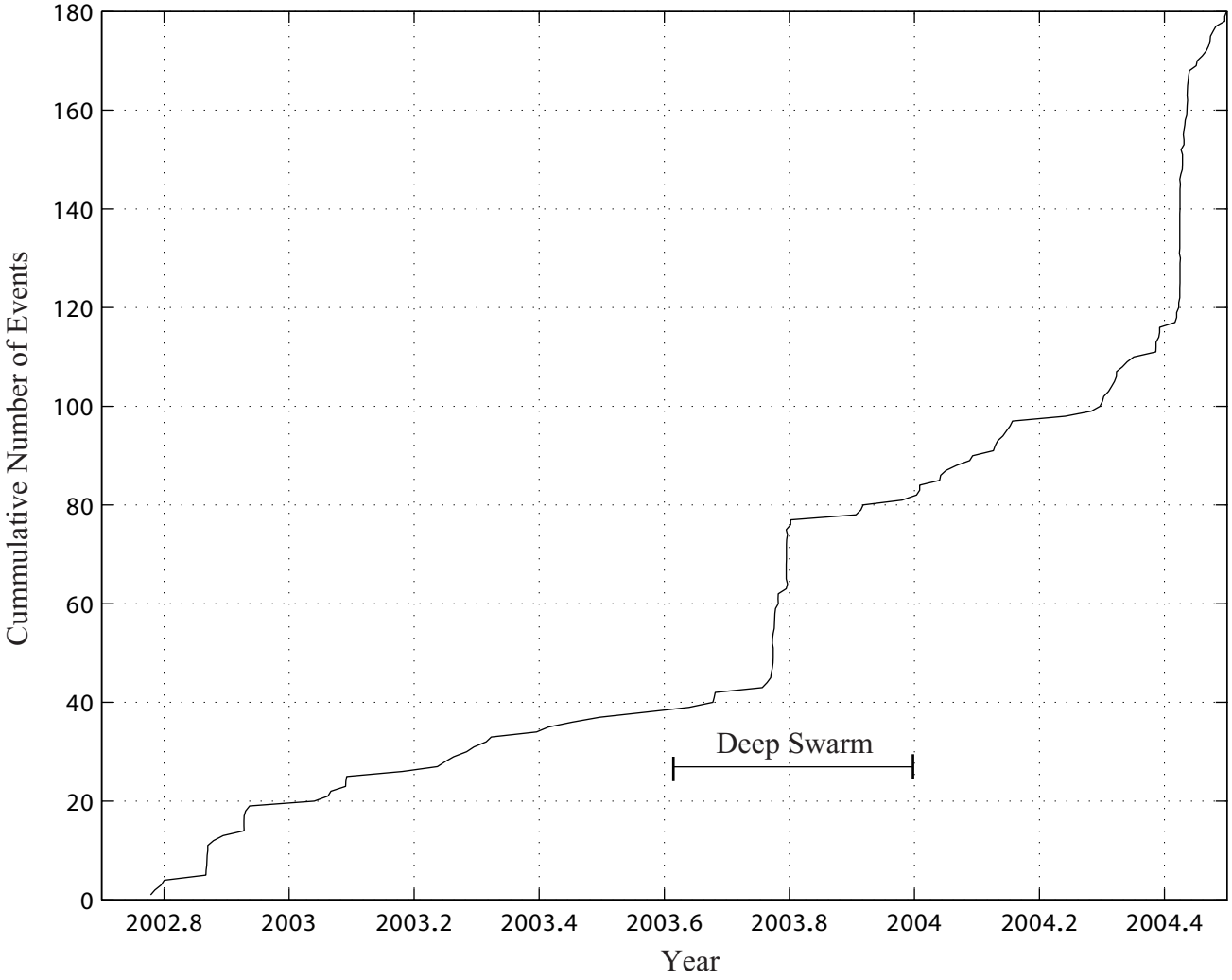

Consistent Detection Threshold (10/1/2002 - 6/30/2004)

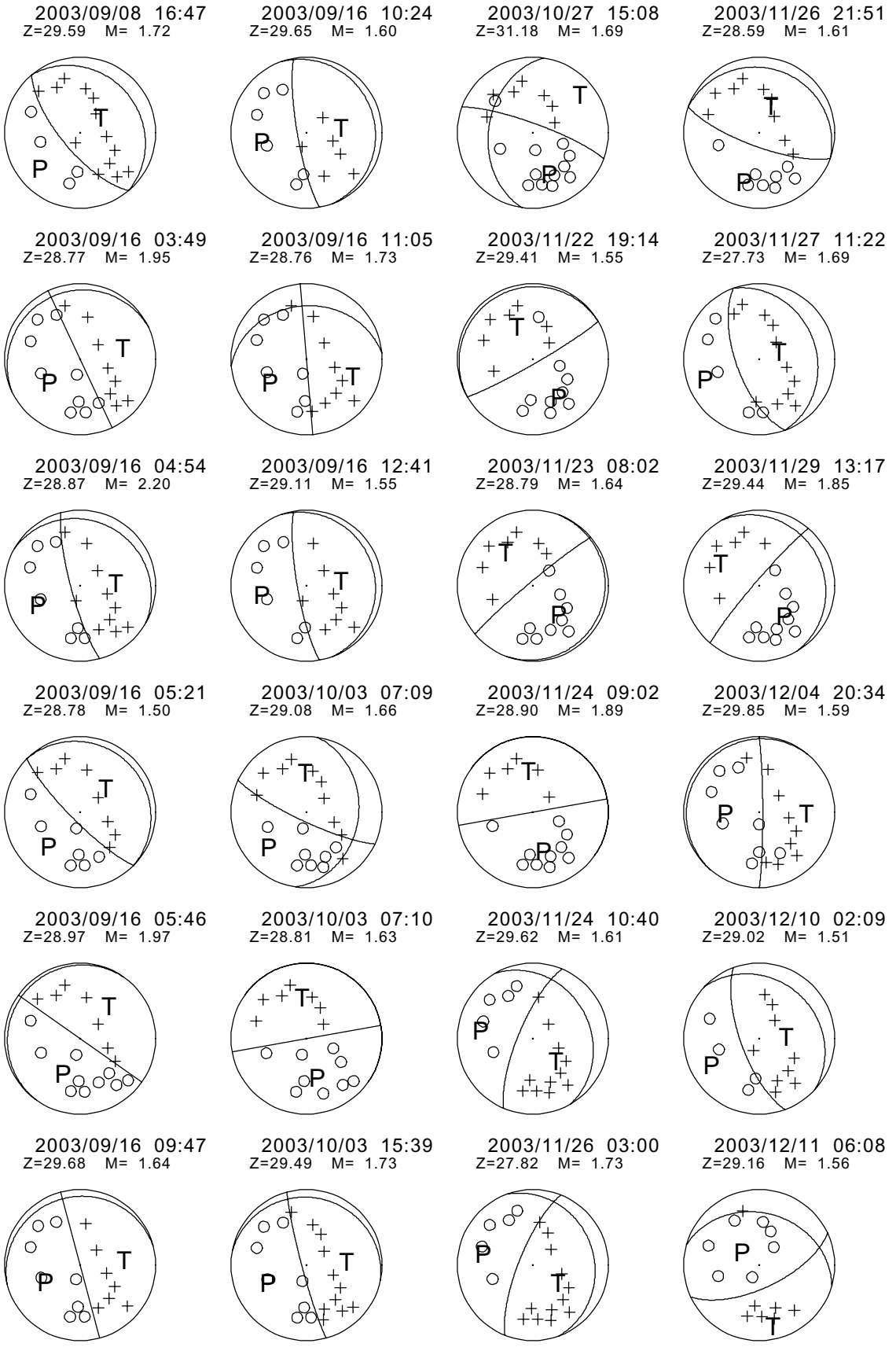
2003/09/08 16:47
Z=29.59 M= 1.72
2003/09/16 10:24
Z=29.65 M= 1.60
2003/10/27 15:08
Z=31.18 M= 1.69
2003/11/26 21:51
Z=28.59 M= 1.61
2003/09/16 03:49
Z=28.77 M= 1.95
2003/09/16 11:05
Z=28.76 M= 1.73
2003/11/22 19:14
Z=29.41 M= 1.55
2003/11/27 11:22
Z=27.73 M= 1.69
2003/09/16 04:54
Z=28.87 M= 2.20
2003/09/16 12:41
Z=29.11 M= 1.55
2003/11/23 08:02
Z=28.79 M= 1.64
2003/11/29 13:17
Z=29.44 M= 1.85
2003/09/16 05:21
Z=28.78 M= 1.50
2003/10/03 07:09
Z=29.08 M= 1.66
2003/11/24 09:02
Z=28.90 M= 1.89
2003/12/04 20:34
Z=29.85 M= 1.59
2003/09/16 05:46
Z=28.97 M= 1.97
2003/10/03 07:10
Z=28.81 M= 1.63
2003/11/24 10:40
Z=29.62 M= 1.61
2003/12/10 02:09
Z=29.02 M= 1.51
2003/09/16 09:47
Z=29.68 M= 1.64
2003/10/03 15:39
Z=29.49 M= 1.73
2003/11/26 03:00
Z=27.82 M= 1.73
2003/12/11 06:08
Z=29.16 M= 1.56

Figure S3

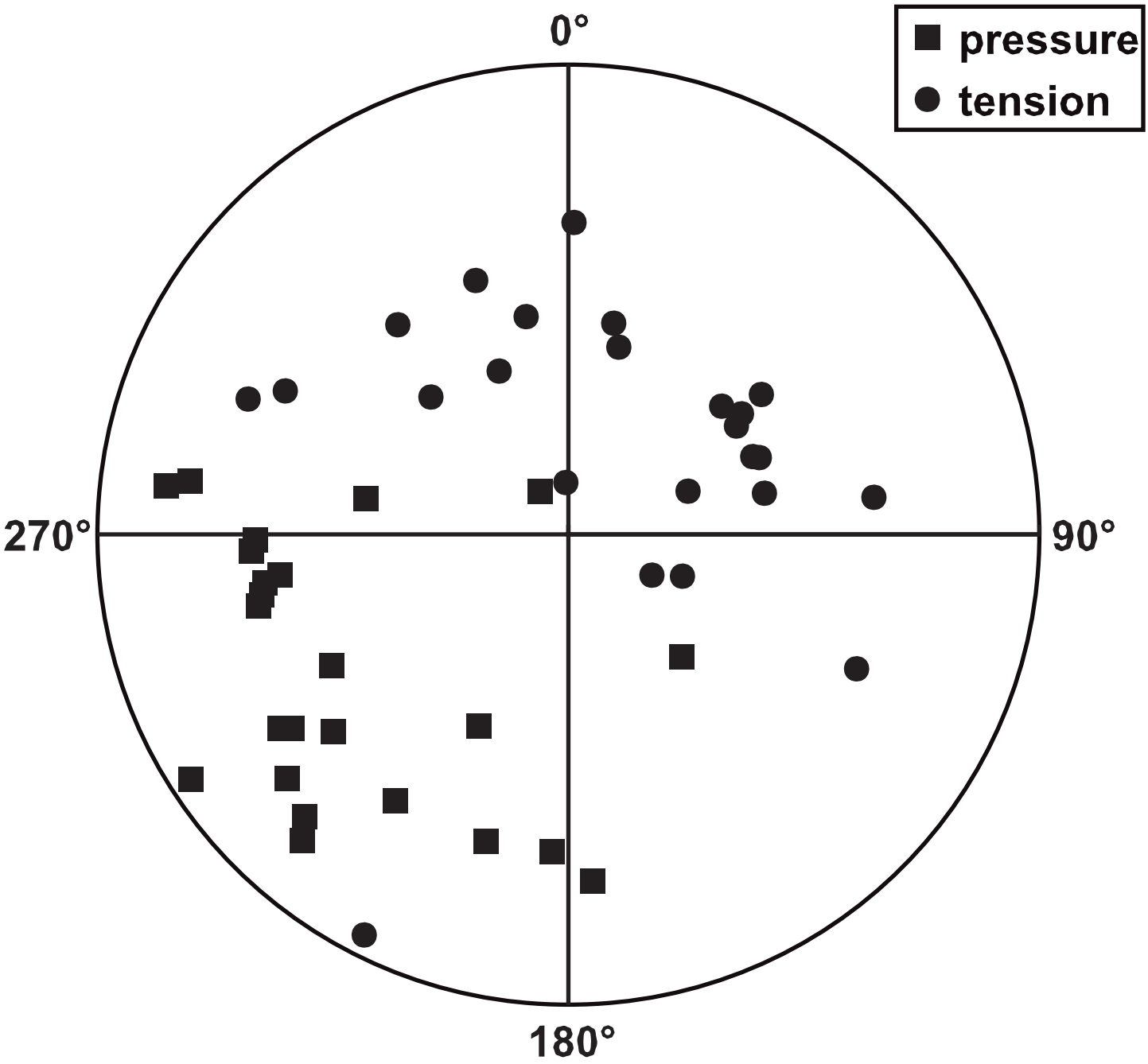

Figure S4